Observing the Galaxy's massive black hole with gravitational wave bursts

C. P. L. Berry[1⋆] and J. R. Gair[1]

[1]*Institute of Astronomy, University of Cambridge, Madingley Road, Cambridge, CB3 0HA*

18 June 2011

ABSTRACT
I thought I would try out the MNRAS LaTeX style.

Key words: black hole physics – Galaxy: centre – gravitational waves – methods: data analysis.

1 BACKGROUND AND INTRODUCTION

Many, if not all, galactic nuclei are believed to have harboured a massive black hole (MBH) during their evolution (Lynden-Bell & Rees 1971; Sołtan 1982; Rees 1984). Observations have shown there exist well-defined correlations between the MBH's mass and the properties of their host galaxies, such as bulge luminosity, mass, velocity dispersion and light concentration (Kormendy & Richstone 1995; Magorrian et al. 1998; Ferrarese & Merritt 2000; Gebhardt et al. 2000; Graham et al. 2001; Tremaine et al. 2002; Marconi & Hunt 2003; Häring & Rix 2004; Graham 2007; Graham et al. 2011). These suggest coeval evolution of the MBH and galaxy, possibly with feedback mechanisms coupling the two (Haiman & Quataert 2004; Volonteri & Natarajan 2009). The MBH and the surrounding spheroidal galaxy share a common history, such that the growth of one can inform us about the growth of the other.

The best opportunity to study MBHs comes from the compact object in our own galactic centre (GC), which is coincident with Sagittarius A* (Sgr A*). This is identified as an MBH of mass $M_\bullet = 4.31 \times 10^6 M_\odot$ at a distance of only $R_0 = 8.33$ kpc (Gillessen et al. 2009).

According to the no-hair theorem, the MBH should be described completely by just its mass $M_\bullet$ and spin a; we expect the charge of an astrophysical black hole to be negligible (Israel 1967, 1968; Carter 1971; Hawking 1972; Robinson 1975; Chandrasekhar 1998). The spin parameter a is related to the BH's angular momentum J by

$$J = M_\bullet a c; \tag{1}$$

it is often convenient to use the dimensionless spin

$$a_* = \frac{cJ}{GM_\bullet^2}. \tag{2}$$

As we have a good estimate of the mass, to gain a full description of the MBH we have only to measure its spin; this

will give us insight into its history and role in the evolution of the Galaxy.

The spin of an MBH is determined by several competing processes. An MBH accumulates mass and angular momentum through accretion (Volonteri 2010). Accretion from a gaseous disc will spin up the MBH, potentially leading to high spin values (Volonteri et al. 2005), while a series of randomly oriented accretion events will lead to a low spin value: we expect an average value $|a_*| \sim 0.1$–0.3 (King & Pringle 2006; King et al. 2008). The MBH will also grow through mergers (Yu & Tremaine 2002; Malbon et al. 2007). Minor mergers with smaller black holes (BHs) can decrease the spin (Hughes & Blandford 2003; Gammie et al. 2004), while a series of major mergers, between similar mass MBHs, would lead to a likely spin of $|a_*| \sim 0.69$ (Berti & Volonteri 2008; Berti et al. 2007; González et al. 2007). Measuring the spin of MBHs will help us understand the relative importance of these processes, and perhaps gain a glimpse into the their host galaxies' pasts.

Elliptical and spiral galaxies are expected to host MBH's of differing spins because of their different evolutions: one expects MBHs in elliptical galaxies to have on average higher spin than black holes in spiral galaxies, where random, small accretion episodes might have played a more important role (Volonteri et al. 2007; Sikora et al. 2007).

It has been suggested that the spin of the Galaxy's MBH could be inferred from careful observation of the orbits of stars within a few milliparsec of the GC (Merritt et al. 2010), although this is complicated because of perturbations due to other stars, or from observations of quasi-periodic oscillations (QPOs) in the luminosity of flares believed to originate from material orbiting close to the inner most stable orbits (Genzel et al. 2003; Bélanger et al. 2006; Trippe et al. 2007; Hamaus et al. 2009; Kato et al. 2010), though there are difficulties in interpreting these results (Psaltis 2008).

This latter method, combined with a disc-seismology model, has produced a value of the dimensionless spin of $a_* = 0.44 \pm 0.08$. To obtain this result Kato et al. (2010) have combined their observations of Sgr A* with observa-

---

⋆ E-mail: cplb2@cam.ac.uk

tions of galactic X-ray sources containing solar mass BHs, to find a best-fit unique spin parameter for all BHs. However, it is not clear that all BHs should share the same value of the spin parameter; especially considering that the BHs considered here differ by six orders of magnitude, with none in the intermediate range. Even if BH spin is determined by a universal process, we would expect some distribution of spin parameters (King et al. 2008; Berti & Volonteri 2008). Thus we cannot precisely determine the spin of the galactic centre's MBH from an average including other BHs.

X-ray observations can be used to infer the spin of MBHs through the observation of Fe K emission lines from active galactic nuclei (Miller 2007; McClintock et al. 2011). So far this has been done for a handful of other galaxies' central MBHs (Brenneman & Reynolds 2006; Miniutti et al. 2009; Schmoll et al. 2009; de la Calle Pérez et al. 2010; Zoghbi et al. 2010; Nardini et al. 2011; Patrick et al. 2011). Estimates for the spin cover a range of values up to the maximal value for an extremal Kerr black hole. Typical values are in the intermediate range of $a_* \sim 0.7$ with an uncertainty of about 10% on each measurement.

While we can use the spin of other BHs as a prior, to inform us of what we should expect to measure for the spin of the Galaxy's MBH, it is desirable to have an independent observation, a direct measurement.

An exciting means of inferring information about the MBH is through gravitational waves (GWs) emitted when compact objects (COs), such as stellar mass BHs, neutron stars (NSs), white dwarfs (WDs) or low mass main sequence (MS) stars, pass close by (Sathyaprakash & Schutz 2009). The proposed Laser Interferometer Space Antenna (LISA) mission is designed to be able to detect GWs in the frequency range of interest for these encounters (Bender et al. 1998; Danzmann & Rüdiger 2003). The identification of waves requires a set of accurate waveform templates covering parameter space. Much work has already been done on the waveforms generated when companion objects inspiral towards an MBH (Glampedakis 2005); as they orbit, the GWs carry away energy and angular momentum, causing the orbit to shrink until eventually the object plunges into the MBH. The initial orbits may be highly elliptical and a burst of radiation is emitted during each close encounter. These are known as extreme mass-ratio bursts (EMRBs; Rubbo et al. 2006). Assuming that the companion is not scattered from its orbit, and does not plunge straight into the MBH, its orbit will evolve, becoming more circular, and it will begin to continuously emit significant gravitational radiation in the LISA frequency range. The resulting signals are known as extreme mass-ratio inspirals (EMRIs; Amaro-Seoane et al. 2007).

Studies of these systems have usually focused upon when the orbit completes multiple cycles, allowing a high signal-to-noise ratio to be accumulated. Here, we will investigate what can be learnt from high eccentricity orbits. These are the initial bursting orbits from which an EMRI may evolve. The event rate for the detection of such EMRBs with LISA has been estimated to be as high as 15 yr^{-1} (Rubbo et al. 2006), although this has been revised downwards to the order of 1 yr^{-1} (Hopman et al. 2007). Even if only a single burst is detected during the LISA mission, this is still an exciting possibility since the information carried by the GW should give an unparalleled probe of the struc-

ture of spacetime of the GC. Exactly what can be inferred will depend upon the orbit.

We will make the simplifying assumption that all these orbits are marginally bound, or parabolic, since highly eccentric orbits will appear almost indistinguishable from an appropriate parabolic orbit. Here "parabolic" and "eccentricity" refer to the energy of the geodesic and not to the geometric shape of the orbit.[1] Following such a trajectory an object may make just one pass of the MBH or, if the periapsis distance is small enough, it may complete a number of rotations. Such an orbit is referred to as zoom-whirl (Glampedakis & Kennefick 2002).

In order to compute the gravitational waveform produced in such a case, we integrate the geodesic equations for a parabolic orbit in Kerr spacetime. We assume that the orbiting body is a test particle, such that it does not influence the underlying spacetime, and that the orbital parameters evolve negligibly during the orbit so that they may be held constant. We use this to construct an approximate numerical kludge waveform (Babak et al. 2007).

This paper is organised as follows. In Sec. 2 we discuss the construction of the geodesic orbits, and in Sec. 3 we explain how to construct a numerical kludge waveform from this trajectory. In Sec. 4 we establish what the LISA detectors would measure, in Sec. 5 how the signal would be analysed to extract the information encoded in the the waveform. [Something else here] In Sec. 8 we confirm the accuracy of the kludge waveforms by comparing the energy flux with fluxes calculated from other approaches. We conclude in Sec. 9 with a summary of our results. An appendix is included on the use of window functions to reduce spectral leakage when analysing waveforms. In this we present a novel window function, the Planck-Bessel window, which may be of use for signals with a large dynamic range.

Throughout this work we will assume metric with signature $(+, -, -, -)$. Greek indices are used to represent spacetime indices $\mu = \{0, 1, 2, 3\}$ and lowercase Latin indices from the middle of the alphabet are used for spatial indices $i = \{1, 2, 3\}$. Uppercase Latin indices from the beginning of the alphabet will be used for the output of two LISA detector-arms $A = \{\mathrm{I}, \mathrm{II}\}$, and lowercase Latin indices from the beginning of the alphabet are used for parameter space. Summation over repeated indices is assumed unless explicitly noted otherwise. Geometric units with $G = c = 1$ will be used where noted, but in general factors of G and c will be retained.

2   PARABOLIC ORBITS IN KERR SPACETIME

2.1   The metric and geodesic equations

Astrophysical BHs are described by the Kerr metric (Kerr 1963). In standard Boyer-Lindquist coordinates the line element is (Boyer & Lindquist 1967; Hobson et al. 2006, section 13.7)

$$\mathrm{d}s^2 = \frac{\rho^2 \Delta}{\Sigma^2} c^2 \mathrm{d}t^2 - \frac{\Sigma \sin^2 \theta}{\rho^2} (\mathrm{d}\phi - \omega \mathrm{d}t)^2 - \frac{\rho^2}{\Delta} \mathrm{d}r^2 - \rho^2 \mathrm{d}\theta^2, \quad (3)$$

---

[1] Marginally bound Keplerian orbits in flat spacetime are parabolic in both senses.

where we have introduced functions

$$\rho^2 = r^2 + a^2 \cos^2\theta, \tag{4}$$

$$\Delta = r^2 - \frac{2GM_\bullet r}{c^2} + a^2, \tag{5}$$

$$\Sigma = \left(r^2 + a^2\right)^2 - a^2 \Delta \sin^2\theta, \tag{6}$$

$$\omega = \frac{2GM_\bullet ar}{c\Sigma}. \tag{7}$$

For the remainder of this section we shall work in natural units with $G = c = 1$.

Geodesics are parameterized by three conserved quantities (aside from the particle's mass μ): energy (per unit mass) E, specific angular momentum about the symmetry axis (the z-axis) L_z, and Carter constant Q (Carter 1968; Chandrasekhar 1998, section 62). The geodesic equations are

$$\rho^2 \frac{dt}{d\tau} = a\left(L_z - aE\sin^2\theta\right) + \frac{r^2 + a^2}{\Delta}T, \tag{8}$$

$$\rho^2 \frac{dr}{d\tau} = \pm\sqrt{V_r}, \tag{9}$$

$$\rho^2 \frac{d\theta}{d\tau} = \pm\sqrt{V_\theta}, \tag{10}$$

$$\rho^2 \frac{d\phi}{d\tau} = \frac{L_z}{\sin^2\theta} - aE + \frac{a}{\Delta}T, \tag{11}$$

where we have introduced potentials

$$T = E\left(r^2 + a^2\right) - aL_z, \tag{12}$$

$$V_r = T^2 - \Delta\left[r^2 + (L_z - aE)^2 + Q\right], \tag{13}$$

$$V_\theta = Q - \cos^2\theta\left[a^2\left(1 - E^2\right) + \frac{L_z^2}{\sin^2\theta}\right], \tag{14}$$

and τ is proper time. The signs of the r and θ equations may be chosen independently.

For a parabolic orbit $E = 1$; the particle is at rest at infinity. This simplifies the geodesic equations. It also allows us to give a simple interpretation for Carter constant Q: this is defined as

$$Q = L_\theta^2 + \cos^2\theta\left[a^2\left(1 - E^2\right) + \frac{L_z^2}{\sin^2\theta}\right], \tag{15}$$

where L_θ is the (non-conserved) specific angular momentum in the θ-direction ($V_\theta = L_\theta^2$). For $E = 1$ we have

$$Q = L_\theta^2 + \cot^2\theta\, L_z^2 = L_\infty^2 - L_z^2, \tag{16}$$

where L_∞ is the total specific angular momentum at infinity, where the metric is asymptotically flat (de Felice 1980).[2] This is as in Schwarzschild spacetime.

2.2 Integration variables and turning points

In integrating the geodesic equations, difficulties can arise because of the presence of turning points in the motion, when the sign of the r or θ geodesic equation will change. The radial turning points are at the periapsis r_p and at infinity. We may locate the periapsis by finding the roots of

$$V_r = 2M_\bullet r^3 - \left(L_z^2 + Q\right)r^2 + 2M_\bullet\left[(L_z - a)^2 + Q\right]r - a^2 Q$$
$$= 0. \tag{17}$$

[2] See Rosquist et al. (2009) for a discussion of the interpretation of Q in the limit $G \to 0$, corresponding to a flat spacetime.

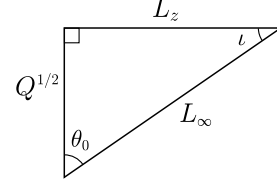**Figure 1.** The angular momenta L_∞, L_z and $\sqrt{Q}$ define a right-angled triangle. The acute angles are θ_0, the extremal value of the polar angle, and ι, the orbital inclination (Glampedakis et al. 2002).

This has three roots, which we shall denote $\{r_1, r_2, r_\mathrm{p}\}$; the periapsis r_p is the largest real root. We do not find the apoapsis as a (fourth) root to this equation as we have removed it by taking $E = 1$ before solving: this turning point can be found by setting the unconstrained expression for V_r equal to zero, and then solving for $E(r)$; taking the limit $r \to \infty$ gives $E \to 1$ (Wilkins 1972).

We may avoid the difficulties of the turning point by introducing an angular variable that always increases with proper time (Drasco & Hughes 2004): inspired by Keplerian orbits, we parameterize our trajectory by

$$r = \frac{p}{1 + e\cos\psi}, \tag{18}$$

where $e = 1$ is the eccentricity and $p = 2r_\mathrm{p}$ is the semilatus rectum. As ψ covers its full range from $-\pi$ to π, r traces out one full orbit from infinity through the periapsis at $\psi = 0$ back to infinity. The geodesic equation for ψ is

$$\rho^2 \frac{d\psi}{d\tau} = \left\{M_\bullet\left[2r_\mathrm{p} - (r_1 + r_2)(1 + \cos\psi)\right.\right.$$
$$\left.\left. + \frac{r_1 r_2}{2r_\mathrm{p}}(1 + \cos\psi)^2\right]\right\}^{1/2}. \tag{19}$$

This may be integrated without problem. Parameterizing an orbit by its periapsis and eccentricity has the additional benefit of allowing easier comparison with its flat-space equivalent (Gair et al. 2005).

The θ motion is usually bounded, with $\theta_0 \leqslant \theta \leqslant \pi - \theta_0$; in the event that $L_z = 0$ the particle follows a polar orbit and θ will cover its full range. The turning points are given by

$$V_\theta = Q - \cot^2\theta\, L_z^2 = 0. \tag{20}$$

Only if $L_z = 0$ may we reach the poles (Wilkins 1972). If we change variable to $\zeta = \cos^2\theta$, we have a maximum value $\zeta_0 = \cos^2\theta_0$ given by

$$\zeta_0 = \frac{Q}{Q + L_z^2} = \frac{Q}{L_\infty^2}. \tag{21}$$

See Fig. 1 for a geometrical visualization. Let us now introduce a second angular variable (Drasco & Hughes 2004)

$$\zeta = \zeta_0 \cos^2\chi. \tag{22}$$

Over one 2π period of χ, θ oscillates over its full range, from its minimum value to its maximum and back. The geodesic equation for χ is

$$\rho^2 \frac{d\chi}{d\tau} = \sqrt{Q + L_z^2}, \tag{23}$$

and may be integrated simply.

3   WAVEFORM CONSTRUCTION

For given angular momenta L_z and Q, and initial starting position, we can calculate the geodesic trajectory. The orbiting body is assumed to follow this track exactly: we ignore evolution due to the radiation of energy and angular momentum, which should be negligible for EMRBs. From this trajectory we calculate the waveform using a semirelativistic approximation (Ruffini & Sasaki 1981): we assume that the particle moves along a geodesic in the Kerr geometry, but radiates as if it were in flat spacetime. This quick-and-dirty technique is known as a numerical kludge (NK), and has been shown to approximate well results computed by more accurate methods (Babak et al. 2007).

3.1   Kludge approximation

Numerical kludge approximations aim to encapsulate the main characteristics of a waveform by using the exact particle trajectory (ignoring inaccuracies from radiative effects and from the particle's self-force), whilst saving on computational time by using approximate waveform generation techniques.

To start, we build an equivalent flat-space trajectory from the Kerr geodesic. This is done by identifying the Boyer-Lindquist coordinates with a set of flat-space coordinates; we consider two choices here:

(i) Identify the Boyer-Lindquist coordinates with flat-space spherical polars $\{r_{\mathrm{BL}}, \theta_{\mathrm{BL}}, \phi_{\mathrm{BL}}\} \rightarrow \{r_{\mathrm{sph}}, \theta_{\mathrm{sph}}, \phi_{\mathrm{sph}}\}$, then define flat-space Cartesian coordinates (Gair et al. 2005; Babak et al. 2007)

$$\boldsymbol{x} = \begin{pmatrix} r_{\mathrm{sph}} \sin\theta_{\mathrm{sph}} \cos\phi_{\mathrm{sph}} \\ r_{\mathrm{sph}} \sin\theta_{\mathrm{sph}} \sin\phi_{\mathrm{sph}} \\ r_{\mathrm{sph}} \cos\theta_{\mathrm{sph}} \end{pmatrix}. \qquad (24)$$

(ii) Identify the Boyer-Lindquist coordinates with flat-space oblate-spheroidal coordinates $\{r_{\mathrm{BL}}, \theta_{\mathrm{BL}}, \phi_{\mathrm{BL}}\} \rightarrow \{r_{\mathrm{ob}}, \theta_{\mathrm{ob}}, \phi_{\mathrm{ob}}\}$ so that the flat-space Cartesian coordinates are

$$\boldsymbol{x} = \begin{pmatrix} \sqrt{r_{\mathrm{ob}}^2 + a^2} \sin\theta_{\mathrm{ob}} \cos\phi_{\mathrm{ob}} \\ \sqrt{r_{\mathrm{ob}}^2 + a^2} \sin\theta_{\mathrm{ob}} \sin\phi_{\mathrm{ob}} \\ r_{\mathrm{ob}} \cos\theta_{\mathrm{ob}} \end{pmatrix}. \qquad (25)$$

These are appealing because in the limit that $G \rightarrow 0$, where the gravitating mass goes to zero, the Kerr metric in Boyer-Lindquist coordinates reduces to the Minkowski metric in oblate-spheroidal coordinates.

In the limit of $a \rightarrow 0$, the two coincide, as they do in the limit of large r_{BL}.

It must be stressed that there is no well motivated argument that either coordinate system must yield an accurate GW; their use is justified *post facto* by comparison with results obtained from more accurate, and computationally intensive, methods (Gair et al. 2005; Babak et al. 2007). The ambiguity in assigning flat-space coordinates reflects the inconsistency of the semi-relativistic approximation: the geodesic trajectory was calculated for the Kerr geometry; by moving to flat spacetime we lose the reason for its existence. However, this inconsistency should not be regarded as a major problem; it is just an artifact of the basic assumption that the shape of the trajectory is important for

determining the character of the radiation, but the curvature of the spacetime in the vicinity of the source is not. By binding the particle to the exact geodesic, we ensure that the kludge waveform has spectral components at the correct frequencies, but by assuming flat spacetime for generation of GWs they will not have the correct amplitudes.

3.2   Quadrupole-octupole formula

Now we have a flat-space particle trajectory $x_{\mathrm{p}}^\mu(\tau)$, we may apply a flat-space wave generation formula. We shall use the quadrupole-octupole formula to calculate the gravitational strain (Bekenstein 1973; Press 1977; Yunes et al. 2008)

$$h^{jk}(t, \boldsymbol{x}) = -\frac{2G}{c^6 r}\left(\ddot{I}^{jk} - 2n_i \dddot{S}^{ijk} + n_i \dddot{M}^{ijk}\right)_{t' = t - r/c}, \quad (26)$$

where an over-dot represents differentiation with respect to time t (and not τ), t' is the retarded time, $r = |\boldsymbol{x} - \boldsymbol{x}_{\mathrm{p}}|$ is the radial distance, $\boldsymbol{n}$ is the radial unit vector, and the mass quadrupole I^{jk}, current quadrupole S^{ijk} and mass octupole M^{ijk} are defined by

$$I^{jk}(t') = \int x'^j x'^k T^{00}(t', \boldsymbol{x}') \, \mathrm{d}^3 x'; \qquad (27)$$

$$S^{ijk}(t') = \int x'^j x'^k T^{0i}(t', \boldsymbol{x}') \, \mathrm{d}^3 x'; \qquad (28)$$

$$M^{ijk}(t') = \frac{1}{c} \int x'^i x'^j x'^k T^{00}(t', \boldsymbol{x}') \, \mathrm{d}^3 x'. \qquad (29)$$

This is correct for a slowly moving source. It is the familiar quadrupole formula (Misner et al. 1973, section 36.10; Hobson et al. 2006, section 17.9), derived from linearized theory, plus the next order terms. For a point mass, the energy-momentum tensor $T^{\mu\nu}$ contains a δ-function which allows easy evaluation of the integrals of the various moments to give

$$I^{jk} = c^2 \mu x_{\mathrm{p}}^j x_{\mathrm{p}}^k; \qquad (30)$$

$$S^{ijk} = c\mu v_{\mathrm{p}}^i x_{\mathrm{p}}^j x_{\mathrm{p}}^k; \qquad (31)$$

$$M^{ijk} = c\mu x_{\mathrm{p}}^i x_{\mathrm{p}}^j x_{\mathrm{p}}^k. \qquad (32)$$

Since we are only interested in GWs, we shall use the transverse-traceless (TT) gauge. The waveform is given in the TT gauge by (Misner et al. 1973, box 35.1)

$$h_{jk}^{\mathrm{TT}} = P_j^l h_{lm} P_k^m - \frac{1}{2} P_{jk} P^{lm} h_{lm}, \qquad (33)$$

where the (spatial) projection operator P_{ij} is

$$P_{ij} = \delta_{ij} - n_i n_j. \qquad (34)$$

4   DETECTION WITH LISA

The LISA detector is a three arm, space-borne laser interferometer (Bender et al. 1998; Danzmann & Rüdiger 2003). The three arms form an equilateral triangle that rotates as the system's centre of mass follows a circular, heliocentric orbit, trailing $20°$ behind the Earth. To describe the detector configuration, and to transform from the MBH coordinate system to those of the detector, we will find it useful to define three coordinate systems: those of the BH at the GC $x_\bullet^i$; ecliptic coordinates centred at the solar system (SS)
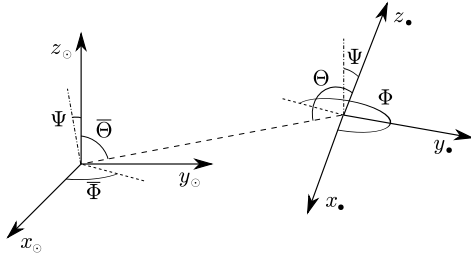
Figure 2. The relationship between the MBH's coordinate system $x_\bullet^i$ and the SS coordinate system $x_\odot^i$. The MBH's spin axis is aligned with the $z_\bullet$-axis.
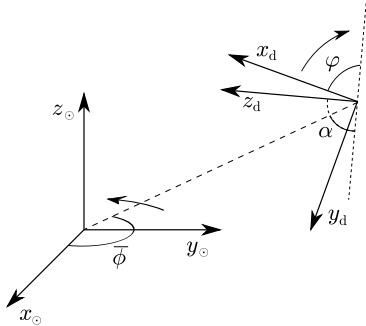

Figure 3. The relationship between the detector coordinates x_d^i and the ecliptic coordinates of the SS $x_\odot^i$ (Bender et al. 1998).

barycentre $x_\odot^i$, and coordinates that co-rotate with the detector x_d^i. The MBH's coordinate system and the SS coordinate system are depicted in Fig. 2. The currently envisioned LISA mission geometry is shown in Fig. 3. We define the detector coordinates such that the detector-arms lie in the x_d-y_d plane as shown in Fig. 4. The coordinate systems are related by a series of angles: Θ and Φ give the orientation of the SS in the MBH's coordinates. These define the orientation of the MBH's spin axis $z_\bullet$. $\overline{\Theta}$ and $\overline{\Phi}$ give the position of the GC in ecliptic coordinates. The angle Ψ specifies the relative inclinations of the z-axes of the SS and MBH: their orientation in the plane of the sky. $\overline{\phi}$ gives LISA's orbital phase and φ gives the rotational phase of the detector arms.
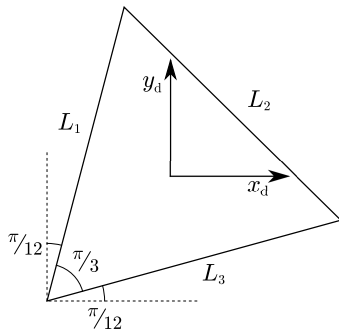

Figure 4. The alignment of the three detector arms, with lengths L_1, L_2 and L_3, within the x_d-y_d plane (Cutler 1998). The origin of the detector coordinates coincides with the centre of mass of the constellation of satellites.

Both of these vary linearly with time

$$\overline{\phi}(t) = \omega_\oplus t + \overline{\phi}_0; \quad \varphi(t) = -\omega_\oplus t + \varphi_0; \tag{35}$$

where $\omega_\oplus$ corresponds to one rotation per year. Finally, $\alpha = 60°$ is the inclination of the detector plane. We have computed the waveforms in the MBH's coordinates, however it is simplest to describe the measured signal using the detector's coordinates.

The strains measured in the three arms can be combined such that LISA behaves as a pair of $90°$ interferometers at $45°$ to each other, with signals scaled by $\sqrt{3}/2$ (Cutler 1998). We will denote the two detectors as I and II. If we label the change in the three arms' lengths caused by GWs δL_1, δL_2 and δL_3, and use L for the unperturbed length, then detector I measures strain

$$h_I(t) = \frac{\delta L_1 - \delta L_2}{L} = \frac{\sqrt{3}}{2}\left(\frac{1}{2}h_d^{xx} - \frac{1}{2}h_d^{yy}\right), \tag{36}$$

and detector II measures

$$h_{II}(t) = \frac{\delta L_1 + \delta L_2 - 2\delta L_3}{\sqrt{3}L} = \frac{\sqrt{3}}{2}\left(\frac{1}{2}h_d^{xy} + \frac{1}{2}h_d^{yx}\right). \tag{37}$$

We will use vector notation $\boldsymbol{h}(t) = (h_I(t), h_{II}(t)) = \{h_A(t)\}$ to represent signals from both detectors.

The final consideration for calculating the signal measured by LISA is the time of arrival of the signal: LISA's orbital position changes with time. Fortunately over the timescales of interest for parabolic encounters, these changes are small. We will assume that the position of the SS barycentre relative to the GC is constant: it is defined by the distance R_0 and the angles $\overline{\Theta}$ and $\overline{\Phi}$. The time of arrival at the SS barycentre $t_\odot$ is then the retarded time; the time of detection t_d to lowest order is

$$t_d \simeq t_\odot - t_{AU} \cos\left[\overline{\phi}(t_\odot) - \overline{\Phi}\right] \sin\overline{\Theta}, \tag{38}$$

where t_{AU} is the light travel-time for LISA's orbital radius. The time t_d is required for $\phi(t)$ and $\varphi(t)$.

5 SIGNAL ANALYSIS

5.1 Frequency domain formalism

Having constructed the GW $\boldsymbol{h}(t)$ that will be incident upon the LISA detector, we may now consider how to analyse the waveform and extract the information it contains. We begin with a brief overview of the basic components of signal analysis used for GWs, with application to LISA in particular. This fixes notation. A more complete discussion of the material can be found in the work of Finn (1992), and Cutler & Flanagan (1994).

The measured strain $\boldsymbol{s}(t)$ will be the combination of the signal and the detector noise

$$\boldsymbol{s}(t) = \boldsymbol{h}(t) + \boldsymbol{n}(t); \tag{39}$$

we will assume that the noise $n_A(t)$ is stationary and Gaussian. When analysing signals, it is most convenient to work with the Fourier transform

$$\tilde{g}(f) = \mathscr{F}\{g(t)\} = \int_{-\infty}^{\infty} g(t)e^{2\pi i f t}\,\mathrm{d}t. \tag{40}$$

For a Gaussian noise signal $n_A(t)$, each Fourier component

$\tilde{n}_A(f)$ also has a Gaussian probability distribution; the assumption of stationarity means that different Fourier components are uncorrelated, thus (Cutler & Flanagan 1994)

$$\langle \tilde{n}_A(f)\tilde{n}_B^*(f') \rangle_n = \frac{1}{2}\delta(f-f')S_{AB}(f), \tag{41}$$

where $\langle \ldots \rangle_n$ denotes the expectation value over the noise distribution, and $S_{AB}(f)$ is the (single-sided) noise spectral density. For simplicity, we may assume that the noise in the two detectors is uncorrelated, but share the same characterisation so that (Cutler 1998)

$$S_{AB}(f) = S_n(f)\delta_{AB}. \tag{42}$$

The functional form of the noise spectral density $S_n(f)$ for LISA is discussed in Sec. 5.2.

The properties of the noise allow us to define a natural inner product and associated distance on the space of signals (Cutler & Flanagan 1994)

$$(\boldsymbol{g}|\boldsymbol{k}) = 2\int_0^\infty \frac{\tilde{g}_A^*(f)\tilde{k}_A(f) + \tilde{g}_A(f)\tilde{k}_A^*(f)}{S_n(f)}\,\mathrm{d}f. \tag{43}$$

Using this definition, the signal-to-noise ratio (SNR) is approximately

$$\rho[\boldsymbol{h}] = (\boldsymbol{h}|\boldsymbol{h})^{1/2}. \tag{44}$$

The probability of a particular realization of noise $\boldsymbol{n}(t) = \boldsymbol{n}_0(t)$ is

$$p(\boldsymbol{n}(t) = \boldsymbol{n}_0(t)) \propto \exp\left[-\frac{1}{2}\left(\boldsymbol{n}_0|\boldsymbol{n}_0\right)\right]. \tag{45}$$

If the incident waveform is given as $\boldsymbol{h}(t)$, the probability of measuring signal $\boldsymbol{s}(t)$ is

$$p(\boldsymbol{s}(t)|\boldsymbol{h}(t)) \propto \exp\left[-\frac{1}{2}\left(\boldsymbol{s}-\boldsymbol{h}|\boldsymbol{s}-\boldsymbol{h}\right)\right]. \tag{46}$$

5.2   LISA noise curve

LISA's noise has two sources: instrumental noise and confusion noise, primarily from white dwarf binaries. The latter may be divided into contributions from galactic and extragalactic binaries. In this work we use the noise model of Barack & Cutler (2004). The shape of the noise curve can be seen in Fig. 5. The instrumental noise dominates at both high and low frequencies. The confusion noise is important at intermediate frequencies, and is responsible for the cusp around $f = 10^{-3}$ Hz.

5.3   Window functions

There is one remaining complication regarding signal analysis: since we are Fourier transforming a finite signal we encounter spectral leakage; a contribution from large amplitude spectral components leaks into surrounding components (sidelobes), obscuring and distorting the spectrum at these frequencies (Harris 1978). This is an inherent problem with finite signals; it will be as much of a problem when analysing signals from LISA as it is computing waveforms here. To mitigate, but unfortunately not eliminate, these effects, the time-domain signal can be multiplied by a window function. These are discussed in detail in Appendix A. We have adopted the Nuttall four-term window with continuous first derivative (Nuttall 1981) for the results presented here.
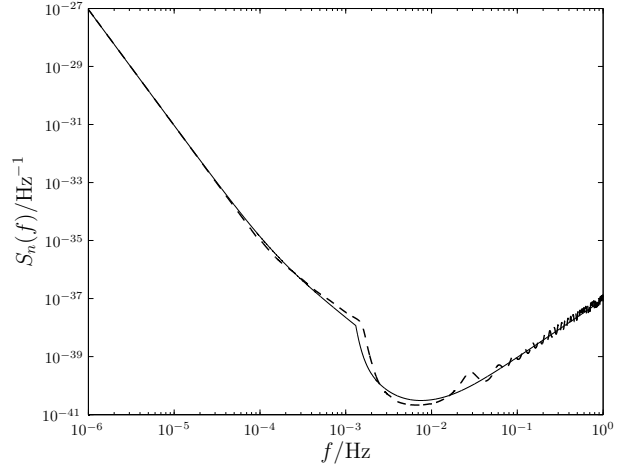

Figure 5. The LISA noise curve. The solid line indicates the analytic approximation of Barack & Cutler (2004) used in this work. For comparison, the dashed line is from the online sensitivity curve generator (http://www.srl.caltech.edu/~shane/sensitivity/; Larson et al. 2000, 2002). For parabolic encounters we are most interested in the low-frequency region where the two curves are the same.

6   PARAMETER ESTIMATION AND WAVEFORMS

6.1   Model parameters

The shape of the waveform depends on a number of parameters: those defining the MBH; those defining the companion object on its orbit, and those defining the LISA detector. Let us define $\boldsymbol{\lambda} = \left\{\lambda^1, \lambda^2, \ldots, \lambda^N\right\}$ as the set of N parameters which specify the GW. For our model, the input parameters are:

(1) The MBH's mass $M_\bullet$. This is currently well constrained by the observation of stellar orbits about Sgr A* (Ghez et al. 2008; Gillessen et al. 2009), with the best estimate being $M_\bullet = (4.31 \pm 0.36) \times 10^6 M_\odot$. However this depends upon the galactic centre distance R_0 being accurately known. If the uncertainty in this is included $M_\bullet = (3.95 \pm 0.06|_{\mathrm{stat}} \pm 0.18|_{R_0,\,\mathrm{stat}} \pm 0.31|_{R_0,\,\mathrm{sys}}) \times 10^6 M_\odot (R_0/8\text{ kpc})^{2.19}$, where the errors are statistical, independent of R_0; statistical from the determination of R_0, and systematic from R_0 respectively.

(2) The spin parameter a_*. Naively this could be anywhere in the range $|a_*| < 1$; however it is possible to place an upper bound by contemplating spin-up mechanisms. Considering the torque from radiation emitted by an accretion disc, and swallowed by the BH, it can be shown that $|a_*| \lesssim 0.998$ (Thorne 1974). Magnetohydrodynamical simulations of accretion discs produce a smaller maximum value of $|a_*| \sim 0.95$ (Gammie et al. 2004). The actual spin value could be much lower than this upper bound depending upon the MBH's evolution (as discussed in Sec. 1). We will use the convention that a_* is positive, and will change the sense of rotation by flipping the z-axis.

(3) The polar angle Θ defining the propagation direction.

(4) The inclination angle Ψ. Since a is positive, this is in the range $[-\pi, \pi]$.

Figure 6. Waveform for model parameters: $a = 0.5M_\bullet$, $\Theta = \pi/3$, $L_z = 3.67M_\bullet$, $Q = 0.409M_\bullet^2$, $x_0 = 3.0 \times 10^{12}$ m, $y_0 = 4.0 \times 10^{12}$ m, $z_0 = 2.0 \times 10^{11}$ m. The periapse distance is $r_{\rm p} = 4.67M_\bullet$, the SNR is $\rho = 8800$.

Figure 7. Waveform for model parameters: $a = 0.5M_\bullet$, $\Theta = \pi/3$, $L_z = 5.22M_\bullet$, $Q = 0.055M_\bullet^2$, , $x_0 = 3.5 \times 10^{12}$ m, $y_0 = 3.5 \times 10^{12}$ m, $z_0 = 1.0 \times 10^{11}$ m. The periapse distance is $r_{\rm p} = 11.77M_\bullet$, the SNR is $\rho = 140$.

Figure 8. Waveform for model parameters: $a = 0.2M_\bullet$, $\Theta = \pi/2$, $L_z = 10.45M_\bullet$, $Q = 2.18M_\bullet^2$, $x_0 = 3.5 \times 10^{12}$ m, $y_0 = 3.5 \times 10^{12}$ m, $z_0 = 5.0 \times 10^{11}$ m. The periapse distance is $r_{\rm p} = 53.7M_\bullet$, the SNR is $\rho = 2.2$.

Figure 9. Waveform for model parameters: $a = 0.7M_\bullet$, $\Theta = \pi/2$, $L_z = 5.22M_\bullet$, $Q = 21.8M_\bullet^2$, $x_0 = 2.8 \times 10^{12}$ m, $y_0 = 2.8 \times 10^{12}$ m, $z_0 = 3.0 \times 10^{12}$ m. The periapse distance is $r_{\rm p} = 22.7M_\bullet$, the SNR is $\rho = 44$.

(5) The SS-GC distance R_0. As for $M_\bullet$, this is constrained by stellar orbits, the best estimate being (Gillessen et al. 2009) $R_0 = 8.33 \pm 0.35$ kpc. We use the logarithm of R_0 in place of R_0.

(6, 7) The coordinates of the MBH from the SS barycentre $\overline{\Theta}$ and $\overline{\Phi}$. These may be taken as the coordinates of Sgr A*, as the radio source is expected to be within ten Schwarzschild radii of the MBH (Reid et al. 2003; Doeleman et al. 2008). At the epoch J2000.0 (Reid et al. 1999) $\overline{\Theta} = 95.607669°$, $\overline{\Phi} = 266.851760°$. This will change with time due to the rotation of the SS about the GC, the proper motion is about $6\,{\rm mas\,yr}^{-1}$, mostly in the plane of the galaxy (Reid et al. 1999; Backer & Sramek 1999; Reid et al. 2003).

(8) The angular momentum of the orbit about the MBH's spin axis L_z.

(9) The Carter constant for the orbit Q.

(10) The mass of the orbiting particle μ. This will depend upon the type of object: whether it is a MS star, WD, NS or BH.

(11–13) The initial position of the particle (x_0, y_0, z_0). For specific values of Q and L_z there is a definite upper limit on $|z_0|/\sqrt{x_0^2 + y_0^2}$ given by the size of θ_0 from (21).

(14, 15) The orbital position of the LISA satellites given by $\overline{\phi}$ and φ. We will assume that the initial positions are chosen such that $\overline{\phi} = 0$ when $\varphi = 0$ (Cutler 1998), however this choice does not qualitatively influence our results.

The azimuthal angle Φ is omitted, since it arbitrarily defines the orientation of the MBH's x- and y-axes. We shall define it to be zero without loss of generality. We have a 15-dimensional parameter space. However, for a given signal arrival time the orbital parameters of LISA will be known; we will not try to infer these.

6.2 Waveforms

Figures 6–10 show example waveforms to demonstrate some of the possible variations in the signal. All these assume $M_\bullet = 8.6 \times 10^{31}$ kg $\simeq 4.3 \times 10^6 M_\odot$, $R_0 = 8.33$ kpc, $\overline{\Theta} = 95.607669°$, $\overline{\Phi} = 266.851760°$ and $\mu = 10^{31}$ kg $\simeq 5M_\odot$; other parameters are specified in the captions. The orbits specified in figures 6, 7 and 9 all loop once about the MBH — they are the simplest zoom-whirl orbits. The others, including the orbit of Fig. **??**, are simpler trajectories that are recognisable as parabolic in shape. There is a clear distinc-

tion between the two types of orbit, as the loops introduce higher frequency harmonics.

The plotted waveforms use the oblate-spheroidal coordinate system for the NK. Using spherical polars makes negligible difference: on the scale shown here the only discernible difference would be in the spikes of the high-frequency tail of the orbits with smaller periapses, and even that is minor. We conclude that the choice of coordinates for the kludge approximation is unimportant, and shall continue using oblate-spheroidal coordinates for the rest of this work.

6.3 Inference and Fisher matrices

Having detected a GW signal $\boldsymbol{s}(t)$, we are interested in what we can learn about the source. We have an inference problem that can be solved by appropriate application of Bayes' Theorem (Jaynes 2003, chapter 4): the probability distribution for our parameters given that we have detected the signal $\boldsymbol{s}(t)$ is given by the posterior

$$p(\boldsymbol{\lambda}|\boldsymbol{s}(t)) = \frac{p(\boldsymbol{s}(t)|\boldsymbol{\lambda})p(\boldsymbol{\lambda})}{p(\boldsymbol{s}(t))}. \tag{47}$$

Here $p(\boldsymbol{s}(t)|\boldsymbol{\lambda})$ is the likelihood of the parameters, $p(\boldsymbol{\lambda})$ is the prior probability distribution for the parameters, and $p(\boldsymbol{s}(t)) = \int p(\boldsymbol{s}(t)|\boldsymbol{\lambda})\,{\rm d}^N\lambda$ is, for our purposes, a normalising constant and may be ignored. The likelihood function depends upon the realization of noise. A particular set of parameters $\boldsymbol{\lambda}_0$ defines a waveform $\boldsymbol{h}_0(t) = \boldsymbol{h}(t; \boldsymbol{\lambda}_0)$, the probability that we observe signal $\boldsymbol{s}(t)$ for this GW is given by (46), so the likelihood is

$$p(\boldsymbol{s}(t)|\boldsymbol{\lambda}_0) \propto \exp\left[-\frac{1}{2}\left(\boldsymbol{s} - \boldsymbol{h}_0|\boldsymbol{s} - \boldsymbol{h}_0\right)\right]. \tag{48}$$

If we were to define this as a probability distribution for the parameters $\boldsymbol{\lambda}$, then the modal values would be the maximum-likelihood parameters $\boldsymbol{\lambda}_{\rm ML}$. The waveform $\boldsymbol{h}(t; \boldsymbol{\lambda}_{\rm ML})$ would be the signal closest to $\boldsymbol{s}(t)$ in the space of all signals, where distance is defined using the inner product (43) (Cutler & Flanagan 1994).

In the limit of a high SNR, we may approximate this as

Figure 10. Waveform for model parameters: $a = 0.7M_\bullet$, $\Theta = \pi/2$, $L_z = 15.7M_\bullet$, $Q = 84.6M_\bullet^2$, $x_0 = 1.0 \times 10^{12}$ m, $y_0 = 4.2 \times 10^{12}$ m, $z_0 = 1.0 \times 10^{12}$ m. The periapse distance is $r_{\rm p} = 148M_\bullet$, the SNR is $\rho = 0.18$.

(Vallisneri 2008)

$$p(\boldsymbol{s}(t)|\boldsymbol{\lambda}_0) \propto \exp\left[-\frac{1}{2}\left(\partial_a \boldsymbol{h}|\partial_b \boldsymbol{h}\right)\left(\lambda^a - \langle\lambda^a\rangle_\ell\right)\left(\lambda^b - \left\langle\lambda^b\right\rangle_\ell\right)\right],$$
(49)

where the mean is defined as

$$\langle\lambda^a\rangle_\ell = \frac{\int \lambda^a p(\boldsymbol{s}(t)|\boldsymbol{\lambda})\,\mathrm{d}^N\lambda}{\int p(\boldsymbol{s}(t)|\boldsymbol{\lambda})\,\mathrm{d}^N\lambda}.$$
(50)

Using the high SNR limit, this is the maximum-likelihood value $\langle\lambda^a\rangle_\ell = \lambda^a_{\mathrm{ML}}$. The quantity

$$\Gamma_{ab} = (\partial_a \boldsymbol{h}|\partial_b \boldsymbol{h})$$
(51)

is the Fisher information matrix. It controls the variance of the likelihood distribution.

The form of the posterior distribution will depend upon the nature of the prior information. If we have an uninformative prior, such that $p(\boldsymbol{\lambda})$ is a constant, then the posterior distribution would be determined by the likelihood. In the high SNR limit, we would obtain a Gaussian with variance-covariance matrix

$$\boldsymbol{\Sigma} = \boldsymbol{\Gamma}^{-1}.$$
(52)

The Fisher information matrix gives the uncertainty associated with the estimated parameter values, in this case the maximum-likelihood values.

If the prior were to restrict the allowed range for a parameter, for example, as is the case for the spin a, then the posterior would be a truncated Gaussian, and $\boldsymbol{\Gamma}^{-1}$ may no longer represent the variance-covariance.

If the prior were approximately Gaussian with variance-covariance matrix $\boldsymbol{\Sigma}_0$, then the posterior would also be Gaussian.[3] The posterior variance-covariance would be (Cutler & Flanagan 1994; Vallisneri 2008)

$$\boldsymbol{\Sigma} = \left(\boldsymbol{\Gamma} + \boldsymbol{\Sigma}_0^{-1}\right)^{-1}.$$
(53)

From this the inverse Fisher matrix $\boldsymbol{\Gamma}^{-1}$ is an upper bound on the size of the posterior covariance matrix.[4]

To understand what we can from parabolic encounters alone, we will look at the inverse Fisher matrix elements. If these are small then we expect we would be able to precisely determine a parameter, whereas if they are large we would not be able to learn much more than we already know from our prior.

7   RESULTS

7.1   Data set

To investigate the variation of inverse Fisher matrix elements for different orbits, waveforms for computed for a

range of different orbits. In each case the massive black hole was assumed to have a mass of $4.31 \times 10^6 M_\odot$, and to be at the J2000.0 coordinates at a distance of 8.33 kpc. Four different spin values were chosen $a_\star = 0, 0.3, 0.6, 0.9$. Waveforms were calculated for two different compact objects, one of mass $1.4 M_\odot$ as appropriate for a neutron star, one of mass $10 M_\odot$ represented a black hole. For each spin and mass, waveforms were computed for orbits with periapses at six different radii, uniformly separated in logarithmic space between $4 r_{\mathrm{S}}$ and $50 r_{\mathrm{S}}$, where $r_{\mathrm{S}} = 2GM_\bullet/c^2$ corresponds to the Schwarzschild radius. At each radii, orbits with three different inclinations $\iota = \pi/12, \pi/4, 5\pi/12$ were calculated, each for both prograde and retrograde rotation. In addition to this, the initial position, orientation of the MBH, and orbital position of LISA were varied: for each combination of MBH spin, compact object mass, periapsis, inclination and rotation sense, 20 random combinations of the remaining parameters were used (each being drawn from a separate uniform distribution over the permitted range).

7.2   Inverse Fisher matrices

From (26) we see that the amplitude of the waveform is proportional to the compact object mass μ. Consequently we expect there to be a proportionality between the SNR and the mass, from (44), $\rho[\boldsymbol{h}] \propto \mu$, and there to be an inverse proportionality between the elements of the variance-covariance matrix and the mass, from (51) and (52), $\Sigma_{ab} \propto \mu^{-2}$. We shall consider mass-scale values to give results independent of the compact object's mass. This will allow an easier combination of results from the computations for a NS and for a BH. From the variance-covariance matrix we can define the uncertainty for a particular parameter

$$\sigma_a = \sqrt{\Sigma_{aa}} \qquad \text{(no summation)}.$$
(54)

This should be proportional to μ^{-1}.

We take the mean of $\ln\sigma$ for each set of 20 randomised parameters (starting position, MBH orientation and LISA orientation).[5]

There exists a correlation between the periapse radius and SNR, as shown in Fig. **??**. Closer orbits produce louder bursts. The straight line is a maximum likelihood fit assuming that the SNR has a Gaussian distribution with standard deviation derived from the scatter of points. The parameter uncertainties are well correlated with the SNR. Some are sensitive to other parameters, such as the MBH spin, or the orbital inclination.

7.3   Junk

There are a few general properties. The parameters $M_\bullet$ and Θ always have relatively small variances. These parameters are crucial for defining the BH system: $M_\bullet$ sets the scale for the system and Θ the orientation. If a were small, the spacetime would be almost spherically symmetric and we would expect a large variance for Θ. The angular momentum L_z

---

[3] If we only know the typical value and spread of a parameter then a Gaussian is the maximum entropy prior (Jaynes 2003, section 7.11): the prior that is least informative given what we do know.

[4] It may also be shown to be the Cramér-Rao bound on the error covariance of an unbiased estimator (Cutler & Flanagan 1994; Vallisneri 2008). Thus it represents the frequentist error: the lower bound on the covariance for an unbiased parameter estimator $\boldsymbol{\lambda}_{\mathrm{est}}$ calculated from an infinite set of experiments with the same signal $\boldsymbol{h}(t)$ but different realisations of the noise $\boldsymbol{n}(t)$.

[5] The logarithm is a better quantity to work with since the standard deviation is a scale parameter that may be distributed over a range of magnitudes (MacKay 2003, chapter 22). Using the median value for σ yields results that are similar quantitatively.

also has a small variance, it is important for specifying the orbit; its partner Q, however, does not always have a small variance, in fact in some cases it has one of the largest. This appears to correlate with the sizes of the covariances of Q: the orbits with the smallest periapses have relatively large covariances for the set of parameters $\{a, Q, z_0\}$, indicating that there is some degeneracy between these. In these cases Q has a much larger variance, as does z_0. The initial coordinates x_0, y_0 and z_0 typically have small variances, the exception being the aforementioned case for z_0.

The parameters with the largest variances are $\overline{\Theta}$ and μ. The large variance of $\overline{\Theta}$ reflects the poor angular resolution of gravitational wave detectors; $\overline{\Phi}$ has a smaller variance as a change in azimuthal position changes the waveform observed in the two detector arms. The particle mass μ has a large variance since it only alters the amplitude of the spectrum and not its shape.

The variances are smaller for larger values of the SNR as is expected. We are able to get such good values from the orbits with small periapses since they have both a high SNR and the distinctive structure of a zoom-whirl orbit.

From this preliminary look at a few example orbits, it appears that we should be able to infer the mass of the Kerr BH at the GC from an EMRB. We can gain information regarding the spin of the MBH if the orbit's periapsis is sufficiently small — we could learn nothing from the orbit of Table **??**. The Fisher matrix analysis suggests that we should be able to accurately infer the spin orientation; however it seems likely that there could be difficulties for small spin values. This will require further investigation. It seems unlikely that we will be able to improve upon our current best estimate for the position of the MBH, but this is already well constrained.

What is particularly exciting is the amount of information we could obtain from a single encounter, which may be all that we would have the opportunity to observe with LISA. Taking the results of Table **??**, which are for an orbit of periapsis $r_\mathrm{p} = 52.7 M_\bullet$, as an example, we could infer maximum-likelihood values $M_\bullet = (4.32 \pm 0.07) \times 10^6 M_\odot$, $a = (0.50 \pm 0.02) M_\bullet$, and $\Theta = (60.0 \pm 1.6)^\circ$. Here we have ignored uncertainty introduced by the error in R_0 which will increase the uncertainty; however, we have also only considered information from GWs and not considered additional information from our prior knowledge: combining these as in (53) would give a smaller posterior variance. While further work will be needed to be certain how much we could expect to learn from EMRBs, this is encouraging.

8 ENERGY SPECTRA

To check that the NK waveforms are sensible, we may compare the energy spectra calculated from these with those obtained from the classic treatment of Peters & Mathews (1963), and Peters (1964). This calculates GW emission for Keplerian orbits in flat spacetime, assuming only quadrupole radiation. The spectrum produced should be similar to that obtained from the NK in weak fields, that is for orbits with a large periapsis; however we do not expect an exact match because of the differing input physics and various approximations.

In addition to using the energy spectrum, we can also use the total energy flux to check the NK waveforms. The total flux contains less information that the spectrum; however results have been calculated for parabolic orbits in Schwarzschild spacetime using time-domain black hole perturbation theory (Martel 2004). These should be more accurate than results calculated using the Peters and Mathews formalism.

We do not intend to use the kludge waveforms to calculate an accurate energy flux: this would be inconsistent as we assume that the orbits do not evolve with time. We only calculate the energy flux as a sanity check, to confirm that the kludge approximation is consistent with other approaches.

8.1 Kludge spectrum

A gravitational wave in the TT gauge has an effective energy-momentum tensor (Misner et al. 1973, section 35.15)

$$T_{\mu\nu} = \frac{c^4}{32\pi G} \left\langle \partial_\mu h_{ij} \partial_\nu h^{ij} \right\rangle, \tag{55}$$

where $\langle \ldots \rangle$ indicates averaging over several wavelengths or periods. The flux of energy through a sphere of radius $r = R$ is

$$\frac{\mathrm{d}E}{\mathrm{d}t} = \frac{c^3}{32\pi G} R^2 \int \mathrm{d}\Omega \left\langle \frac{\mathrm{d}h_{ij}}{\mathrm{d}t} \frac{\mathrm{d}h^{ij}}{\mathrm{d}t} \right\rangle, \tag{56}$$

with $\int \mathrm{d}\Omega$ representing integration over all solid angles. From (26) we see that the waves have a $1/r$ dependence; if we define

$$h_{ij} = \frac{H_{ij}}{r}, \tag{57}$$

we see that, using (26), the flux is independent of R, as required for energy conservation, and

$$\frac{\mathrm{d}E}{\mathrm{d}t} = \frac{c^3}{32\pi G} \int \mathrm{d}\Omega \left\langle \frac{\mathrm{d}H_{ij}}{\mathrm{d}t} \frac{\mathrm{d}H^{ij}}{\mathrm{d}t} \right\rangle. \tag{58}$$

If we now integrate to find the total energy emitted we obtain

$$E = \frac{c^3}{32\pi G} \int \mathrm{d}\Omega \int_{-\infty}^{\infty} \mathrm{d}t \frac{\mathrm{d}H_{ij}}{\mathrm{d}t} \frac{\mathrm{d}H^{ij}}{\mathrm{d}t}. \tag{59}$$

Since we are considering all time, the localization of the energy is no longer of importance and it is unnecessary to average over several periods. Switching to Fourier representation $\widetilde{H}_{ij}(f) = \mathscr{F}\{H_{ij}(t)\}$,

$$E = \frac{\pi c^3}{4G} \int \mathrm{d}\Omega \int_0^{\infty} \mathrm{d}f \, f^2 \widetilde{H}^{ij}(f) \widetilde{H}_{ij}^*(f), \tag{60}$$

using the fact that the signal is real so $\widetilde{H}_{ij}^*(f) = \widetilde{H}_{ij}(-f)$. From this we identify the energy spectrum as

$$\frac{\mathrm{d}E}{\mathrm{d}f} = \frac{\pi c^3}{4G} \int \mathrm{d}\Omega \, f^2 \widetilde{H}^{ij}(f) \widetilde{H}_{ij}^*(f). \tag{61}$$

8.2 Peters and Mathews spectrum

To calculate the Peters and Mathews energy spectrum for a parabolic orbit, we use the limiting result of Turner (1977)

$$\frac{\mathrm{d}E}{\mathrm{d}f} = \frac{4\pi^2}{5} \frac{G^3}{c^5} \frac{M_\bullet^2 \mu^2}{r_\mathrm{p}^2} \left\{ \left[\frac{8f^2}{f_\mathrm{c}^2} B \left(\frac{f}{f_\mathrm{c}} \right) - \frac{2f}{f_\mathrm{c}} A \left(\frac{f}{f_\mathrm{c}} \right) \right]^2 \right.$$
$$\left. + \left(\frac{128f^4}{f_\mathrm{c}^4} + \frac{4f^2}{3f_\mathrm{c}^2} \right) \left[A \left(\frac{f}{f_\mathrm{c}} \right) \right]^2 \right\}, \tag{62}$$

Figure 11. Energy spectra for a parabolic orbit of a $\mu = 10^{31}$ kg $\simeq 5M_\odot$ object about a $M_\bullet = 8.8 \times 10^{36}$ kg $\simeq 4.3 \times 10^6 M_\odot$ Schwarzschild MBH with $L_z = 12M_\bullet$ and $Q = 0$; the periapse distance is $r_{\rm p} = 69.9M_\bullet$. The spectra calculated from a the NK waveform is shown by the solid line and the Peters and Mathews flux is indicated by the dashed line. The NK waveform only uses the quadrupole formula.

where $f_{\rm c}$ is the orbital frequency of a circular orbit of radius equal to $r_{\rm p}$,

$$f_{\rm c} = \frac{1}{2\pi}\sqrt{\frac{G(M_\bullet + \mu)}{r_{\rm p}^3}}, \tag{63}$$

and functions $A\left(\widetilde{f}\right)$ and $B\left(\widetilde{f}\right)$ are defined in terms of Bessel functions. Their precise forms are (Berry & Gair 2010)

$$A\left(\widetilde{f}\right) = \frac{1}{\pi}\sqrt{\frac{2}{3}}K_{1/3}\left(\frac{2^{3/2}\widetilde{f}}{3}\right); \tag{64}$$

$$B\left(\widetilde{f}\right) = \frac{1}{\sqrt{3}\pi}\left[K_{-2/3}\left(\frac{2^{3/2}\widetilde{f}}{3}\right) + K_{4/3}\left(\frac{2^{3/2}\widetilde{f}}{3}\right)\right.$$
$$\left. - \frac{1}{\sqrt{2}\widetilde{f}}K_{1/3}\left(\frac{2^{3/2}\widetilde{f}}{3}\right)\right], \tag{65}$$

where $K_\nu(z)$ is a modified Bessel function of the second kind. This result should be accurate to $\sim 10\%$ for orbits with periapse radii larger than $\sim 10r_{\rm S}$, where $r_{\rm S}$ is the MBH's Schwarzschild radius (Berry & Gair 2010).

8.3 Comparison

Two energy spectra are plotted in Fig. 11 for orbits with a periapsis of $r_{\rm p} = 35.0r_{\rm S}$. For consistency with the approximation of Peters and Mathews the NK waveform has been calculated using only the quadrupole formula. The two spectra appear to be in good agreement, showing the same general shape. The NK spectrum is more tightly peaked, but is always within a factor of 2 (ignoring the high-frequency tail).

Comparing the total energy fluxes, ratios of the various energies are plotted in Fig. 12. The ratios all tend to one in the weak field, as required, but differences become more pronounced in the strong field. The NK energy is larger than the Peters and Mathews result $E_{\rm PM}$: since this only assumes quadrupole radiation, we have only plotted it against the quadrupole NK energy $E_{\rm NK(Q)}$. This behaviour has been seen before for high eccentricity orbits about a non-spinning BH (Gair et al. 2005). It may be explained by considering the total amount of rotation for the different orbits: the Peters and Mathews spectrum assumes a Keplerian orbit, so the total rotation is $\Delta\phi = 2\pi$; the orbit in Kerr geometry rotates more than this (the angle would be 2π in the limit of an infinite periapse, whereas for a periapse small enough that the orbit shows zoom-whirl behaviour, the total angle may be many times 2π). The greater rotation leads to increased emission of gravitational waves and a larger energy flux (Berry & Gair 2010). As expected, there appears

to be reasonable correlation between the amount of rotation $2\pi/\Delta\phi$ and the ratio of energies.

Error in the NK energy compared with the time-domain black hole perturbation theory results of Martel comes form two sources: the neglecting of higher order multipole contributions and the ignoring of background curvature. The contribution of the former can be estimated by looking at the difference in the NK energy by including the current quadrupole and mass octupole terms. Form Fig. 12 we see that these terms give a negligible contribution in the weak field, but the difference is $\sim 20\%$ in the strong field. This explains why the Martel energy $E_{\rm M}$ is greater in the strong field, as it includes contributions from all multipoles. Neglecting the background curvature increases the NK energy relative to $E_{\rm M}$. This partially cancels out the error introduced by not including higher order terms: this accidentally leads to $E_{\rm NK(Q)}$ being more accurate than $E_{\rm NK}$ for $r_{\rm p} \sim 12r_{\rm S}$ (Tanaka et al. 1993).

From the level of agreement we may be confident that the NK waveforms are a reasonable approximation. The difference in energy flux is only greater than 10% for very strong fields $r_{\rm p} \simeq 2r_\odot S$; since this is dependent on the square of the waveform, typical accuracy in the waveform may be $\sim 5\%$ (Gair et al. 2005; Tanaka et al. 1993).

9 DISCUSSION

We have outlined an approximate method of generating gravitational waveforms for EMRBs originating at the GC. This assumes that the orbits are parabolic and employs a numerical kludge approximation. The two coordinate schemes for a NK presented here yield almost indistinguishable results. We conclude that either is a valid choice for this purpose.

The waveforms created appear to be consistent with results obtained using Peters and Mathews waveforms for large periapses, indicating that they have the correct weak-field form. The NK approach should be superior to that of Peters and Mathews in the strong-field regime as it uses the exact geodesics of the Kerr spacetime.

Using the NK waveforms we have conducted a trial investigation, using Fisher matrix analysis, into how accurately we could infer parameters of the galactic centre's MBH should such an EMRB be observed. Potentially, it is possible to determine very precisely the key parameters defining the MBH's mass and spin, if the orbit gets close enough to the black hole. Unfortunately, it is necessary to use a prior for the distance to the GC because of a large degeneracy with the compact object's mass, and we are unable to place significantly stricter constraints on this value.

From our investigation it appears that we can achieve good results from a single EMRB with periapsis of $r_{\rm p} = 50M_\bullet$. This translates to a distance of 10^{11} m or 10^{-5} pc.

Before we can quote results for how accurately we can determine the various parameters, we must consider the probability of each orbit. This will be the subject of a future paper, building upon the earlier results of Rubbo et al. (2006) and Hopman et al. (2007), who only considered the probability for a signal to be detectable. Using a model for the galactic centre it is possible to define distributions for angular momenta L_z and Q, for a species of mass μ. With
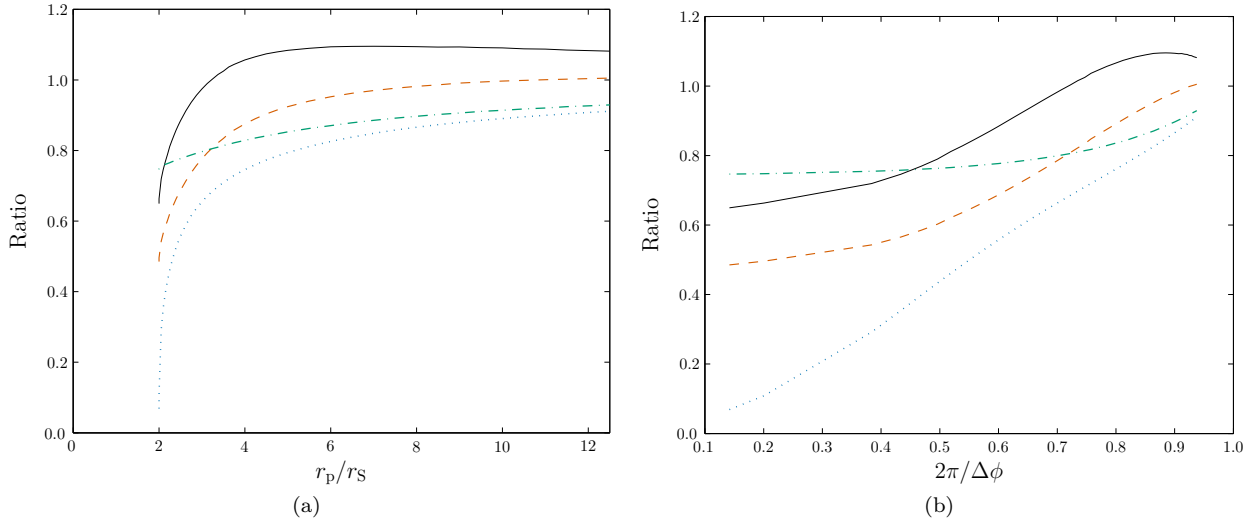
(a)   (b)

Figure 12. Ratios of energies as a function of periapsis r_p and 2π divided by the total angle of rotation in one orbit $\Delta\phi$ ($2\pi/\Delta\phi = 1$ for a Keplerian orbit). The solid line shows the ratio of the numerical kludge and Martel energies E_{NK}/E_M; the dashed line shows the ratio of the NK energy calculated using only the quadrupole term and the Martel energy $E_{NK(Q)}/E_M$; the dot-dashed line shows the ratio of the quadrupole and quadrupole-octupole NK energies $E_{NK(Q)}/E_{NK}$, and the dotted line shows the ratio of the Peters and Mathews and quadrupole NK energies $E_{PM}/E_{NK(Q)}$.

these it is possible to estimate the event rate, and define an expectation value for the elements of the variance-covariance matrix $\mathbf{\Sigma}$. This would describe how much information, on average, we could hope to obtain from EMRB observations.

It will also be necessary to consider on which orbits MS stars would survive without being tidally disrupted (Kobayashi et al. 2004).

Some consideration should also be given to methods of fitting a waveform to an observed signal. Given an input signal, what is the best algorithm for finding the optimal set of parameters to characterise the observed waveform? It is necessary to consider this to check if there are degenerate combinations of parameters that produce similar waveforms; if these are sufficiently distinct in parameter space we would not be aware of them by only considering the region immediately about the ML point. In this work we have assumed that we can correctly identify the waveform's parameters. We do not intend to use NK waveforms to actually identify real GWs: more accurate methods should be employed for that; the point of this study would be to identify potential pitfalls that could be encountered when using accurate waveforms.

We could extend the simple Fisher matrix analysis performed here to a full Bayesian analysis with the distributions for L_z, Q, μ, x_0, y_0 and z_0 serving as priors. However this may be too computationally expensive to justify implementing.

A natural continuation of this work would be to consider EMRBs from other MBHs. LISA should be able to detect EMRBs originating from the Virgo cluster (Rubbo et al. 2006), however the detectable rate may be only 10^{-4} yr^{-1} per galaxy (Hopman et al. 2007). It would be interesting to check what we could expect to infer about MBHs in other galaxies from GWs.

REFERENCES

Amaro-Seoane P., Gair J. R., Freitag M., Miller M. C., Mandel I., Cutler C. J., Babak S., 2007, Classical and Quantum Gravity, 24, R113

Babak S., Fang H., Gair J., Glampedakis K., Hughes S., 2007, Physical Review D, 75, 024005

Backer D. C., Sramek R. A., 1999, The Astrophysical Journal, 524, 805

Barack L., Cutler C., 2004, Physical Review D, 69, 082005

Bekenstein J. D., 1973, The Astrophysical Journal, 183, 657

Bélanger G., Terrier R., de Jager O. C., Goldwurm A., Melia F., 2006, Journal of Physics: Conference Series, 54, 420

Bender P., Brillet A., Ciufolini I., Cruise A. M., Cutler C., Danzmann K., 1998, Technical report, LISA Pre-Phase A Report. Max-Planck-Institut für Quantenoptik, Garching

Berry C. P. L., Gair J. R., 2010, Physical Review D, 82, 107501

Berti E., Cardoso V., Gonzalez J. A., Sperhake U., Hannam M., Husa S., Brügmann B., 2007, Physical Review D, 76, 064034

Berti E., Volonteri M., 2008, The Astrophysical Journal, 684, 822

Boyer R. H., Lindquist R. W., 1967, Journal of Mathematical Physics, 8, 265

Brenneman L. W., Reynolds C. S., 2006, The Astrophysical Journal, 652, 1028

Burko L. M., Khanna G., 2007, EPL, 78, 60005

Carter B., 1968, Physical Review, 174, 1559

Carter B., 1971, Physical Review Letters, 26, 331

Chandrasekhar S., 1998, The Mathematical Theory of Black Holes. Oxford Classic Texts in the Physical Sciences, Oxford University Press, Oxford

Cutler C., 1998, Physical Review D, 57, 7089

Cutler C., Flanagan E. E., 1994, Physical Review D, 49,

2658

Damour T., Iyer B. R., Sathyaprakash B. S., 2000, Physical Review D, 62, 084036

Danzmann K., Rüdiger A., 2003, Classical and Quantum Gravity, 20, S1

de Felice F., 1980, Journal of Physics A: Mathematical and General, 13, 1701

de la Calle Pérez I., Longinotti A. L., Guainazzi M., Bianchi S., Dovčiak M., Cappi M., Matt G., Miniutti G., Petrucci P. O., Piconcelli E., Ponti G., Porquet D., Santos-Lleó M., 2010, Astronomy & Astrophysics, 524, A50

Doeleman S. S., Weintroub J., Rogers A. E. E., Plambeck R., Freund R., 2008, Nature, 455, 78

Drasco S., Hughes S., 2004, Physical Review D, 69, 044015

Ferrarese L., Merritt D., 2000, The Astrophysical Journal, 539, L9

Finn L. S., 1992, Physical Review D, 46, 5236

Gair J. R., Kennefick D. J., Larson S. L., 2005, Physical Review D, 72, 084009

Gammie C. F., Shapiro S. L., McKinney J. C., 2004, The Astrophysical Journal, 602, 312

Gebhardt K., Bender R., Bower G., Dressler A., Faber S. M., Filippenko A. V., Green R., Grillmair C., Ho L. C., Kormendy J., Lauer T. R., Magorrian J., Pinkney J., Richstone D., Tremaine S., 2000, The Astrophysical Journal, 539, L13

Genzel R., Schödel R., Ott T., Eckart A., Alexander T., Lacombe F., Rouan D., Aschenbach B., 2003, Nature, 425, 934

Ghez A. M., Salim S., Weinberg N. N., Lu J. R., Do T., Dunn J. K., Matthews K., Morris M. R., Yelda S., Becklin E. E., Kremenek T., Milosavljevic M., Naiman J., 2008, The Astrophysical Journal, 689, 1044

Gillessen S., Eisenhauer F., Trippe S., Alexander T., Genzel R., Martins F., Ott T., 2009, The Astrophysical Journal, 692, 1075

Glampedakis K., 2005, Classical and Quantum Gravity, 22, S605

Glampedakis K., Hughes S., Kennefick D., 2002, Physical Review D, 66, 064005

Glampedakis K., Kennefick D., 2002, Physical Review D, 66, 044002

González J. A., Sperhake U., Brügmann B., Hannam M., Husa S., 2007, Physical Review Letters, 98, 091101

Graham A. W., 2007, Monthly Notices of the Royal Astronomical Society, 379, 711

Graham A. W., Erwin P., Caon N., Trujillo I., 2001, The Astrophysical Journal, 563, L11

Graham A. W., Onken C. A., Athanassoula E., Combes F., 2011, Monthly Notices of the Royal Astronomical Society, 412, 2211

Haiman Z., Quataert E., 2004, The Formation and Evolution of the First Massive Black Holes. Kluwer Academic Publishers, Dordrecht, pp 147–186

Hamaus N., Paumard T., Müller T., Gillessen S., Eisenhauer F., Trippe S., Genzel R., 2009, The Astrophysical Journal, 692, 902

Häring N., Rix H.-W., 2004, The Astrophysical Journal, 604, L89

Harris F., 1978, Proceedings of the IEEE, 66, 51

Hawking S. W., 1972, Communications in Mathematical Physics, 25, 152

Hobson M. P., Efstathiou G., Lasenby A., 2006, General Relativity: An Introduction for Physicists. Cambridge University Press, Cambridge

Hopman C., Freitag M., Larson S. L., 2007, Monthly Notices of the Royal Astronomical Society, 378, 129

Hughes S. A., Blandford R. D., 2003, The Astrophysical Journal, 585, L101

Israel W., 1967, Physical Review, 164, 1776

Israel W., 1968, Communications in Mathematical Physics, 8, 245

Jaynes E. T., 2003, Probability Theory: The Logic of Science. Cambridge University Press, Cambridge

Kaiser J., Schafer R., 1980, Acoustics, Speech and Signal Processing, IEEE Transactions on, 28, 105

Kato Y., Miyoshi M., Takahashi R., Negoro H., Matsumoto R., 2010, Monthly Notices of the Royal Astronomical Society: Letters, 403, L74

Kerr R., 1963, Physical Review Letters, 11, 237

King A. R., Pringle J. E., 2006, Monthly Notices of the Royal Astronomical Society: Letters, 373, L90

King A. R., Pringle J. E., Hofmann J. A., 2008, Monthly Notices of the Royal Astronomical Society, 385, 1621

Kobayashi S., Laguna P., Phinney E. S., Meszaros P., 2004, The Astrophysical Journal, 615, 855

Kormendy J., Richstone D., 1995, Annual Review of Astronomy and Astrophysics, 33, 581

Larson S. L., Hellings R. W., Hiscock W. A., 2002, Physical Review D, 66, 062001

Larson S. L., Hiscock W. A., Hellings R. W., 2000, Physical Review D, 62, 062001

Lynden-Bell D., Rees M. J., 1971, Monthly Notices of the Royal Astronomical Society, 152, 461

McClintock J. E., Narayan R., Davis S. W., Gou L., Kulkarni A., Orosz J. A., Penna R. F., Remillard R. A., Steiner J. F., 2011, Classical and Quantum Gravity, 28, 114009

MacKay D. J. C., 2003, Information Theory, Inference and Learning Algorithms. Cambridge University Press, Cambridge

McKechan D. J. A., Robinson C., Sathyaprakash B. S., 2010, Classical and Quantum Gravity, 27, 084020

Magorrian J., Tremaine S., Richstone D., Bender R., Bower G., Dressler A., Faber S. M., Gebhardt K., Green R., Grillmair C., Kormendy J., Lauer T., 1998, The Astronomical Journal, 115, 2285

Malbon R. K., Baugh C. M., Frenk C. S., Lacey C. G., 2007, Monthly Notices of the Royal Astronomical Society, 382, 1394

Marconi A., Hunt L. K., 2003, The Astrophysical Journal, 589, L21

Martel K., 2004, Physical Review D, 69, 044025

Merritt D., Alexander T., Mikkola S., Will C. M., 2010, Physical Review D, 81, 062002

Miller J., 2007, Annual Review of Astronomy and Astrophysics, 45, 441

Miniutti G., Panessa F., De Rosa A., Fabian A. C., Malizia A., Molina M., Miller J. M., Vaughan S., 2009, Monthly Notices of the Royal Astronomical Society, 398, 255

Misner C. W., Thorne K. S., Wheeler J. A., 1973, Gravitation. W. H. Freeman, New York

Nardini E., Fabian A. C., Reis R. C., Walton D. J., 2011, Monthly Notices of the Royal Astronomical Society, 410, 1251

Nuttall A., 1981, IEEE Transactions on Acoustics, Speech and Signal Processing, 29, 84

Patrick A. R., Reeves J. N., Porquet D., Markowitz A. G., Lobban A. P., Terashima Y., 2011, Monthly Notices of the Royal Astronomical Society, 411, 2353

Peters P. C., 1964, Physical Review, 136, B1224

Peters P. C., Mathews J., 1963, Physical Review, 131, 435

Press W., 1977, Physical Review D, 15, 965

Psaltis D., 2008, Living Reviews in Relativity, 11

Rees M. J., 1984, Annual Review of Astronomy and Astrophysics, 22, 471

Reid M. J., Menten K. M., Genzel R., Ott T., Schödel R., Brunthaler A., 2003, Astronomische Nachrichten, 324, 505

Reid M. J., Readhead A. C. S., Vermeulen R. C., Treuhaft R. N., 1999, The Astrophysical Journal, 524, 816

Robinson D., 1975, Physical Review Letters, 34, 905

Rosquist K., Bylund T., Samuelsson L., 2009, International Journal of Modern Physics D, 18, 429

Rubbo L. J., Holley-Bockelmann K., Finn L. S., 2006, The Astrophysical Journal, 649, L25

Ruffini R., Sasaki M., 1981, Progress of Theoretical Physics, 66, 1627

Sathyaprakash B., Schutz B. F., 2009, Living Reviews in Relativity, 12

Schmoll S., Miller J. M., Volonteri M., Cackett E., Reynolds C. S., Fabian A. C., Brenneman L. W., Miniutti G., Gallo L. C., 2009, The Astrophysical Journal, 703, 2171

Sikora M., Stawarz Ł., Lasota J.-P., 2007, The Astrophysical Journal, 658, 815

Sołtan A., 1982, Monthly Notices of the Royal Astronomical Society, 200, 115

Tanaka T., Shibata M., Sasaki M., Tagoshi H., Nakamura T., 1993, Progress of Theoretical Physics, 90, 65

Thorne K. S., 1974, The Astrophysical Journal, 191, 507

Tremaine S., Gebhardt K., Bender R., Bower G., Dressler A., Faber S. M., Filippenko A. V., Green R., Grillmair C., Ho L. C., Kormendy J., Lauer T. R., Magorrian J., Pinkney J., Richstone D., 2002, The Astrophysical Journal, 574, 740

Trippe S., Paumard T., Ott T., Gillessen S., Eisenhauer F., Martins F., Genzel R., 2007, Monthly Notices of the Royal Astronomical Society, 375, 764

Turner M., 1977, The Astrophysical Journal, 216, 610

Vallisneri M., 2008, Physical Review D, 77, 042001

Volonteri M., 2010, The Astronomy and Astrophysics Review, 18, 279

Volonteri M., Madau P., Quataert E., Rees M. J., 2005, The Astrophysical Journal, 620, 69

Volonteri M., Natarajan P., 2009, Monthly Notices of the Royal Astronomical Society, 400, 1911

Volonteri M., Sikora M., Lasota J.-P., 2007, The Astrophysical Journal, 667, 704

Wilkins D., 1972, Physical Review D, 5, 814

Yu Q., Tremaine S., 2002, Monthly Notices of the Royal Astronomical Society, 335, 965

Yunes N., Sopuerta C. F., Rubbo L. J., Holley-Bockelmann K., 2008, The Astrophysical Journal, 675, 604

Zoghbi A., Fabian A. C., Uttley P., Miniutti G., Gallo L. C., Reynolds C. S., Miller J. M., Ponti G., 2010, Monthly Notices of the Royal Astronomical Society, 401, 2419

[htbp]

Figure A1. Example spectra calculated using a rectangular window. The high-frequency tail is the result of spectral leakage. The input parameters are: $M_\bullet = 4.3 \times 10^6 M_\odot$, $a = 0.5M_\bullet$, $\Theta = \pi/3$, $\Phi = 0$, $R_0 = 8.33$ kpc, $\bar{\Theta} = 95.607669°$, $\bar{\Phi} = 266.851760°$, $\bar{\phi}_0 = 0$, $\varphi_0 = 0$, $L_z = 10.44M_\bullet$, $Q = 0.055M_\bullet^2$, $\mu = 5M_\odot$, $x_0 = 3.5 \times 10^{12}$ m, $y_0 = 3.0 \times 10^{12}$ m, $z_0 = 1.0 \times 10^{11}$ m; see Sec. 6.1 for a discussion of these parameters. The periapse distance is $r_{\rm p} = 52.7M_\bullet$. The high-frequency tail is the result of spectral leakage. The level of the LISA noise curve is indicated by the dashed line. The calculated SNR is $\rho = 11$.

APPENDIX A: WINDOW FUNCTIONS

When we perform a Fourier transform using a computer we must necessarily only transform a finite time-span τ. The effect of this is the same as transforming the true, infinite signal multiplied by a unit top-hat function of width equal to the time-span. Fourier transforming this yields the true waveform convolved with a sinc. If $\tilde{h}'(f)$ is the computed Fourier transform then

$$\tilde{h}'(f) = \int_{-\tau/2}^{\tau/2} h(t)e^{2\pi i f t}\,\mathrm{d}t = \left[\tilde{h}(f) * \tau\,\mathrm{sinc}(\pi f \tau)\right], \quad \text{(A1)}$$

where $\tilde{h}(f) = \mathscr{F}\{h(t)\}$ is the unwindowed Fourier transform of the infinite signal. This windowing of the data is a problem inherent in the method and results in spectral leakage.

Figure A1 shows the computed Fourier transforms for an example parabolic encounter. The waveforms have two distinct regions: a low-frequency curve, and a high-frequency tail. The low-frequency signal is the spectrum we are interested in; the high-frequency components are the result of spectral leakage. The $\mathcal{O}(1/f)$ behaviour of the sinc gives the shape of the tail. This has possibly been misidentified in figure 8 of Burko & Khanna (2007) as the characteristic strain for parabolic encounters.

Despite being many orders of magnitude below the peak level, the high-frequency tail is still well above the noise curve for a wide range of frequencies. It therefore contributes to the evaluation of any inner products, and could mask interesting features. It is possible to reduce the amount of leakage using apodization: to improve the frequency response of a finite time series one can use a weighting window function $w(t)$ which modifies the impulse response in a prescribed way. The simplest window function is the rectangular (or Dirichlet) window $w_{\rm R}(t)$; this is just the top-hat described above. Other window functions are generally tapered.[6] There is a wide range of window functions described in the literature (Harris 1978; Kaiser & Schafer 1980; Nuttall 1981; McKechan et al. 2010). The introduction of a window function influences the spectrum in a manner dependent upon its precise shape; there are two distinct distortions: local smearing due to the finite width of the centre lobe, and distant leakage due to finite amplitude sidelobes. The window function may be optimised such that the

---

[6] When using a tapered window function it is important to ensure that the window is centred upon the signal; otherwise the calculated transform will have a reduced amplitude.

peak sidelobe has a small amplitude, or such that the side-lobes decay away rapidly with frequency. Choosing a window function is a trade-off between these various properties, and will depend upon the particular application.

For use with the parabolic spectra, the primary concern is to suppress the sidelobes. Many windows with good side-lobe behaviour exist in the literature, we will consider three: the Blackman-Harris minimum four-term window (Harris 1978; Nuttall 1981)

$$w_{\mathrm{BH}}(t) = \sum_{n=0}^{3} a_n^{\mathrm{BH}} \cos\left(\frac{2n\pi t}{\tau}\right), \tag{A2}$$

where

$$\begin{aligned} a_0^{\mathrm{BH}} &= 0.35875, \quad a_1^{\mathrm{BH}} = 0.48829, \\ a_2^{\mathrm{BH}} &= 0.14128, \quad a_3^{\mathrm{BH}} = 0.01168; \end{aligned} \tag{A3}$$

the Nuttall four-term window with continuous first derivative (Nuttall 1981)

$$w_{\mathrm{N}}(t) = \sum_{n=0}^{3} a_n^{\mathrm{N}} \cos\left(\frac{2n\pi t}{\tau}\right), \tag{A4}$$

where

$$\begin{aligned} a_0^{\mathrm{N}} &= 0.355768, \quad a_1^{\mathrm{N}} = 0.487396, \\ a_2^{\mathrm{N}} &= 0.144232, \quad a_3^{\mathrm{N}} = 0.012604, \end{aligned} \tag{A5}$$

and the Kaiser-Bessel window (Harris 1978; Kaiser & Schafer 1980)

$$w_{\mathrm{KB}}(t;\beta) = \frac{I_0\left[\beta\sqrt{1-(2t/\tau)^2}\right]}{I_0(\beta)}, \tag{A6}$$

where $I_\nu(z)$ is the modified Bessel function of the first kind, and β is an adjustable parameter. Increasing β reduces the peak sidelobe, but also widens the central lobe. The Kaiser-Bessel window has the smallest peak sidelobe, but the worst decay ($1/f$); the Nuttall window has best the best asymptotic behaviour ($1/f^3$); the Blackman-Harris window has a peak sidelobe similar to the Nuttall window, and decays asymptotically as fast (slow) as the Kaiser-Bessel window, but has the advantage of having suppressed sidelobes next to the central lobe. Another window has been recently suggested for use with gravitational waveforms: the Planck-taper window (Damour et al. 2000; McKechan et al. 2010)

$$w_{\mathrm{P}}(t;\epsilon) = \begin{cases} \dfrac{1}{\exp(Z_+)+1} & -\dfrac{\tau}{2} \leqslant t < -\tau\left(\dfrac{1}{2}-\epsilon\right) \\ 1 & -\tau\left(\dfrac{1}{2}-\epsilon\right) < t < \tau\left(\dfrac{1}{2}-\epsilon\right), \\ \dfrac{1}{\exp(Z_-)+1} & -\tau\left(\dfrac{1}{2}-\epsilon\right) < t \leqslant \dfrac{\tau}{2} \end{cases} \tag{A7}$$

with

$$Z_\pm(t;\epsilon) = 2\epsilon\left[\frac{1}{1\pm 2(t/\tau)} + \frac{1}{1-2\epsilon\pm 2(t/\tau)}\right]. \tag{A8}$$

This was put forward for use with binary coalescences, and has superb asymptotic decay. However, the peak sidelobe is high, which could be disadvantageous for this application. We therefore propose a new window function: the Planck-Bessel window which simply combines the Kaiser-Bessel and
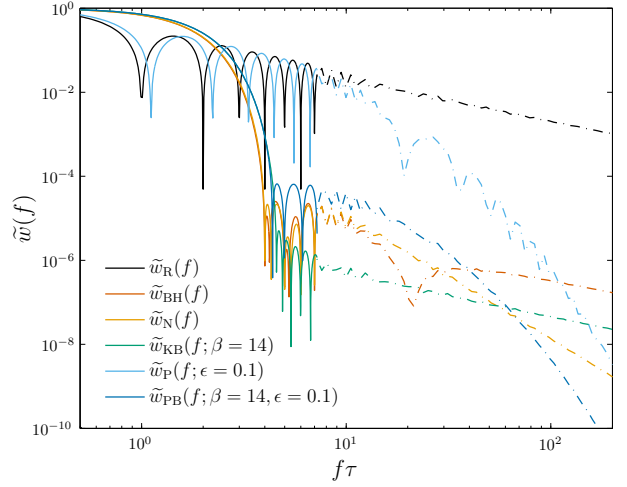

Figure A2. Window function frequency response. To avoid clutter, the response function is only plotted in detail until $f\tau = 8$, above this a smoothed value is used, as indicated by the dot-dashed line. As well as having good asymptotic behaviour, the Planck-taper window has the narrowest main lobe, except for the rectangular window.

[htbp]

Figure A3. Example spectra calculated using (a) a rectangular window and (b) Nuttall's four-term window with continuous first derivative (Nuttall 1981). The input parameters are: $M_\bullet = 3.3 \times 10^6 M_\odot$, $a = 0.5 M_\bullet$, $\Theta = \pi/3$, $\Phi = 0$, $R_0 = 8.33$ kpc, $\overline{\Theta} = 95.607669°$, $\overline{\Phi} = 266.851760°$, $\overline{\phi}_0 = 0$, $\varphi_0 = 0$, $L_z = 10.44 M_\bullet$, $Q = 0.055 M_\bullet^2$, $\mu = 5 M_\odot$, $x_0 = 3.5 \times 10^{12}$ m, $y_0 = 3.0 \times 10^{12}$ m, $z_0 = 1.0 \times 10^{11}$ m; see Sec. 6.1 for a discussion of these parameters. The periapse distance is $r_{\mathrm{P}} = 52.7 M_\bullet$. The high-frequency tail is the result of spectral leakage. The level of the LISA noise curve is indicated by the dashed line. The spectra are from detector I, detector II has similar spectra.

Planck-taper windows to produce a window which inherits the best features of both, albeit in a diluted form

$$w_{\mathrm{PB}}(t;\beta,\epsilon) = w_{\mathrm{P}}(t;\epsilon)w_{\mathrm{KB}}(t;\beta). \tag{A9}$$

The window functions' frequency responses are plotted in Fig. A2. There is no window that performs best everywhere.

Figure A3 shows the computed Fourier transforms for an example parabolic encounter using no window (alternatively a rectangular or Dirichlet window), and the Nuttall four-term window with continuous first derivative.[7] The waveforms have two distinct regions: a low-frequency curve, and a high-frequency tail. The low-frequency signal is the spectrum we are interested in; the high-frequency components are the result of spectral leakage. Using the Nuttall window, the spectral leakage is greatly reduced; the peak sidelobe is lower, and the tail decays away as $1/f^3$ instead of $1/f$.

The choice of window function will influence the results

---

[7] The Blackman-Harris minimum four-term window, the Kaiser-Bessel window and the Planck-Bessel window give almost identical results.

as it changes the form of $\widetilde{h}(f)$. The variation in results between windows depends upon the signal: variation is greatest for low frequency bursts, as then there is greatest scope for leakage into the LISA frequency band; variation is least significant for zoom-whirl orbits as then there are strong signals to relatively high frequencies, and spectral leakage is confined to mostly below the noise level. To quantify the influence of window functions, we studied the diagonal elements of the Fisher matrix from a selection of orbits with periapsis ranging from $\sim 10M_\bullet$–$300M_\bullet$. For orbits with small periapses all five windows (excluding the rectangular window) produced very similar results: the Planck-taper window differed by a maximum of $\sim 0.5\%$ from the others, which all agreed to better than 0.1%. The worst case results came from the lowest frequency orbits, then the Planck-taper window deviated by a maximum of $\sim 30\%$ in the value for the Fisher matrix elements, the Blackman-Harris deviated by $\sim 20\%$ and the others agreed to better than $\sim 5\%$. The Planck-taper window's performance is limited by its poor sidelobe behaviour; the Blackman-Harris has the worst performance at high frequency.

For this work we have used the Nuttal window. Its performance is comparable to the Kaiser-Bessel and Planck-Bessel windows; however it is computationally less expensive to implement as it does not contain Bessel functions. Results should be accurate to a few percent at worst, and results from closer orbits, which provide better constraints, should be less affected by the choice of window function. Therefore, we are confident that none of our conclusions is sensitive to the particular windowing method implemented.

This paper has been typeset from a TEX/ LATEX file prepared by the author.